Patterned Laser Ablation of Microgrooves with Controllable Cross-Sections

Pei Qiu, Yang Guo, Lingyu Huang, Jun Li, Jiaxu Huang, Min Wang, Zhiyu Zhang,* and Shaolin Xu*

Fabricating precision microgrooves with controllable cross-sections on difficult-to-machine materials is significantly valuable but still challenging. Herein, a patterned laser-induced microjet-assisted ablation method for cross-sectional profiles controllable laser micromachining is proposed. During the liquid-assisted laser ablation process, debris and bubbles that may disturb the laser energy deposition can be instantaneously expelled by a directional laser-induced microjet. The Gaussian laser spot is spatially modulated into specific geometric shapes, such as triangles, to tune locally deposited laser energy to carve microgrooves with designed cross-sections. To achieve customized microgrooves efficiently, a reliable geometrical model based on the ablation threshold theory is developed to guide the processing parameter selection, including the laser spot shape, polarization, pulse energy, and scanning strategies. The simulation and experimental results confirm that this method achieves the decoupled control of the groove depth and width in a single-path laser ablation process. Using this method, the design and manufacturing of microgrooves with controllable cross-sections on single crystalline silicon carbide are demonstrated. The patterned laser-induced microjet-assisted ablation method provides a new route for fabricating precision microgrooves with controllable cross-sections on difficult-to-machine materials.

1. Introduction

Precision machining of microstructures on hard-to-machine materials is primarily important for high-added-value manufacturing. Third-generation semiconductors as emerging hard-to-machine materials are excellent materials for the further development of optical-electric industry due to their extraordinary physical properties, such as wide band gap, high refractive index, and high thermal conductivity. These virtues lay their unique foundation in broad application fields like high-threshold optical elements, micro-heat sinks, and micro-electromechanical systems.[1–5] Those devices usually require elaborately designed surface microstructures to achieve desired functions. For example, high damage threshold blazed gratings composed of parallel microgrooves with controllable angles are needed to achieve maximum diffraction efficiency in a designed diffraction order.[6] Heat transfer or dissipation performance of heat sinks and sensitivity of gas proportional counter detectors also benefit from designable microgroove cross-sections.[7–9] However, fabricating those designed microgrooves, especially on these hard-to-machine third-generation semiconductors, is still a long-pending challenge in modern manufacturing industries.

Ultrafast laser micromachining has recently attracted growing attention for the fabrication of microgrooves with the virtue of low material selectivity and environment friendliness.[10–12] The researchers try to investigate techniques to control the cross-section of microgroove by ultrafast laser. For example, the V-shape and U-shape microgroove can be achieved by varying the laser focal plane.[13] Groove shapes can also be adjusted by pulse energy or scanning strategy.[14] Notably, the controllability of the geometrical features of microgrooves is highly restricted if simply utilizing an unmodulated Gaussian beam. The depth and width of the microgrooves change simultaneously when altering the pulse energy and pulse overlap ratio, making it very difficult to apply a Gaussian beam to achieve the decoupled control of the width and depth of microgrooves. Various shaped apertures and the computer-generated holograms generated by the Gale-Shapley algorithm are commonly used wavefront modulation methods, which can transform the Gaussian laser beam into arbitrary shapes for laser ablation.[15–18] But the redeposition of ablation debris hinders the material removal and causes structural

P. Qiu, Y. Guo, L. Huang, J. Li, J. Huang, S. Xu
Department of Mechanical and Energy Engineering
Southern University of Science and Technology
Shenzhen 518055, China
E-mail: xusl@sustech.edu.cn

M. Wang
School of Microelectronics
Southern University of Science and Technology
Shenzhen 518055, China

Z. Zhang
Key Laboratory of Optical System Advanced Manufacturing Technology
Changchun Institute of Optics, Fine Mechanics and Physics
Chinese Academy of Sciences
Changchun 130033, China
E-mail: zhangzhiyu@ciomp.ac.cn

**ADVANCED
SCIENCE NEWS**

www.advancedsciencenews.com

**ADVANCED
MATERIALS
TECHNOLOGIES**

www.advmattechnol.de

quality decline, which is another stubborn problem of ultrafast laser micromachining in an atmospheric environment.[19] Thus, currently reported patterned laser ablation methods are still not flexible and efficient in fabricating microgrooves precisely.

Various endeavors have been groped to conquer those challenges in laser micromachining. Liquid-assisted laser ablation has been proven feasible to expel ablation debris in the ablation zone.[20–22] However, due to the extremely high fluence of the laser, it will break down the liquid and generate cavitation bubbles in the liquid-assisted laser ablation. Laser-induced cavitation bubbles generally expand outward randomly, leading to liquid turbulence and hindering laser beam transmission.[23–25] Some works suggest that thin liquid film acts particularly well in assisting laser ablation.[26,27] When a thin liquid film is employed in laser ablation, the laser-induced cavitation bubble will experience an asymmetric collapse due to the boundary effect, which generally causes a fast liquid ejection, namely a laser-induced microjet.[28–32] This laser-induced microjet helps to eliminate ablative products and to avoid the scattering of bubbles in liquid-assisted laser micromachining. Based on this principle, a new laser-induced microjet-assisted ablation (LIMJAA) technique has been proposed for high-quality microfabrication.[33]

Eliminating the disturbance from unexpected scatters, like debris and bubbles, allows the ablated groove to be fully controlled by the local laser energy deposition. Here, we exploit a patterned LIMJAA approach for processing microgrooves with high accuracy and controllable cross-sections. A laser beam with a specific intensity profile is applied during the ablation process, which is modulated via a patterned phase mask loaded on a spatial light modulator (SLM).[34] A geometrical model considering laser polarization for cross-sectional profile prediction is established and experimentally verified, helping to guide microgroove manufacturing. Benefit from the digitally shaped laser beam, separately controlling the depth and width of microgrooves in a decoupled way is achieved. Furthermore, various microgrooves profiles are also successfully demonstrated through our method, including asymmetric, symmetric, and even hierarchical grooves.

2. Results and Discussion

2.1. Principle of Patterned LIMJAA

We developed the patterned LIMJAA method, as shown in **Figure 1**a. Since the thickness of the liquid film in the stable area is as small as 35.4 μm, the laser can induce a continuous microjet opposite to the laser scanning direction. The continuous microjet will instantaneously take ablation debris and secondary bubbles away from the ablation area, making the patterned laser ablation process much more stable.[33]

Figure 1b,c shows the experimental comparison between laser micromachining in air and LIMJAA in a thin liquid film, where an asymmetrical triangular laser spot is conducted for ablation. The cross-sectional profile of the microgroove ablated in air is close to a parabolic shape instead of desired asymmetrical triangular. Mass of ablation debris stacks at the laser ablation zone during laser ablation in air, and the ablative debris in the microgroove cannot be removed even after ultrasonic cleaning. Unlike laser ablation in air, which is subjected to splashing and recasting of ablation products, LIMJAA can instantly remove ablation prod-

ucts. Thus, a microgroove almost free of debris is obtained, and its profile is consistent with the designed laser spot pattern, as shown in Figure 1c.

It can be seen that the ablation depth in air is shallower than that in a liquid film under the same processing parameters. We further studied the ablation results of microgrooves by low-speed single-scanning and high-speed multi-scanning as depicted in Figures S1 and S2, Supporting Information, respectively. As long as ablation debris deposits in the groove, it results in uncontrollable micromachining. Thus, avoiding the interference of ablative debris is necessary for cross-section controllable ablation. Figure 1d shows oblique gratings by patterned LIMJAA, which proves the stability of the patterned LIMJAA method.

In the process of Gaussian laser scanning ablation, the effective pulse number (N) is calculated as[35]

$$N = \frac{D \cdot f}{v} \tag{1}$$

where D is the laser beam spot diameter, f is the laser repetition frequency, and v is the laser scanning speed. In this study, the Gaussian laser spot is spatially reshaped, so we defined a new parameter called locally-deposited effective pulse number (N_e), namely the effective pulse number in different locations of the shaped laser spot, which is linear to the spot features $h(x)$ along the scanning direction as shown in Figure 1b and can be calculated by

$$N_e(x) = \frac{h(x) \cdot f}{v} \tag{2}$$

The ablation depth of the microgroove is dominantly determined by deposited energy per unit area in the patterned LIMJAA process. The total deposited energy per unit area is calculated by the single pulse energy times N_e, which is linearly related to $h(x)$, so the microgroove profile can be controlled by designing the spot shape.

2.2. Guidelines on Laser Spot Pattern Design for Controllable Cross-Sections

As revealed in Figure 1c, the cross-sectional profile of the microgroove is highly correlated to the shape of the laser spot in LIMJAA, making it feasible to control the profile of ablated grooves by tuning the spot shape. Here, we first established a geometrical model for predicting the cross-sectional profiles of grooves based on an ablation threshold model.[36]

In the model, the ablation depth (L) is calculated according to the laser fluence $F(x,y)$ at a specific position (x,y):

$$L(x,y) = \delta \ln \frac{F(x,y)}{F_{th}} \tag{3}$$

where δ is the thermal penetration depth of the target material,[37,38] F_{th} is the ablation threshold of the material. The ablation threshold will decrease due to an incubation effect of multiple pulses, as described in the formula $F_{th}(N) = F_{th}(1)N^{S-1}$,[39] where $F_{th}(N)$ is multi-shot threshold fluence, N is the number of pulses, $F_{th}(1)$ is the ablation threshold for a single pulse and S is
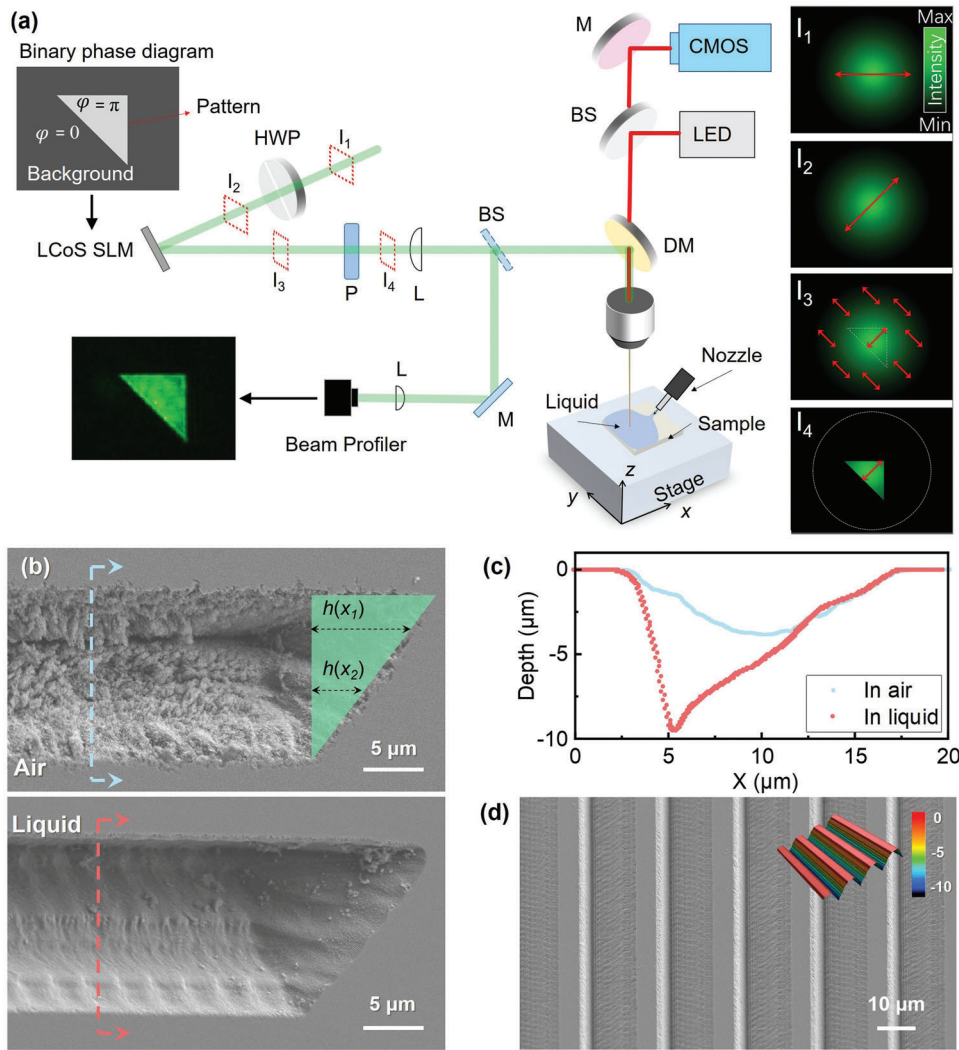
ADVANCED
SCIENCE NEWS

www.advancedsciencenews.com

ADVANCED
MATERIALS
TECHNOLOGIES

www.advmattechnol.de

Figure 1. a) Schematic diagram of the experimental setup and patterned laser-induced microjet-assisted ablation; I_1-I_4 on the upright corner are schematics of light intensity distributions and polarization states (red double arrows) at the corresponding positions in the optical path diagram (HWP: half waveplate, P: polarizer, BS: beam splitter, M: mirror, DM: dichroic mirror). The morphology of microgrooves processed in air and liquid film is presented in (b). c) Comparison of the cross-sectional profiles of microgrooves processed in air and thin liquid film. d) Morphology and 3D profiles of parallel microgroove arrays. All microgrooves are fabricated with laser repetition frequency f = 5 kHz, laser energy E = 8 µJ, and scanning speed v = 100 µm s^{-1}.

the incubation coefficient. As shown in Figure S3 and Table S1, Supporting Information, $F_{th}(1)$ is 0.56 J cm^{-2} and S is 0.82 when SiC is ablated by the femtosecond laser with a liquid film.

The fluence distribution in the focal plane satisfies the Gaussian function:

$$F_0 \ (x, y) = \frac{2E_p}{\pi \omega_0^2} e^{-\frac{2(x^2 + y^2)}{\omega_0^2}} \tag{4}$$

where ω_0 is the beam radius (at e^{-2} laser intensity of the maximum laser intensity), and E_p is the pulse energy.

As the laser beam is shaped by an SLM, any shape of the laser spot can be generated. In this new geometrical model, the profile of the binary phase diagram is extracted to define the spot. Thus, a window function $\tau(x, y)$ is introduced to redefine the original

energy distribution,

$$\tau \ (x, y) = \begin{cases} 1, \varphi = \pi \\ 0, \varphi = 0 \end{cases} \tag{5}$$

So the laser fluence in the focal plane is described by

$$F \ (x, y) = \frac{2E_p}{\pi \omega_0^2} e^{-\frac{2(x^2+y^2)}{\omega_0^2}} \tau \ (x, y) \tag{6}$$

In addition, the reflectance coefficients of lasers are affected by laser polarization and incident angles. Larger incident angles lead to more significantly different reflectance between s- and p-polarization components. Using the classical Fresnel formulas, the comprehensive reflectance R_c by considering the polarization
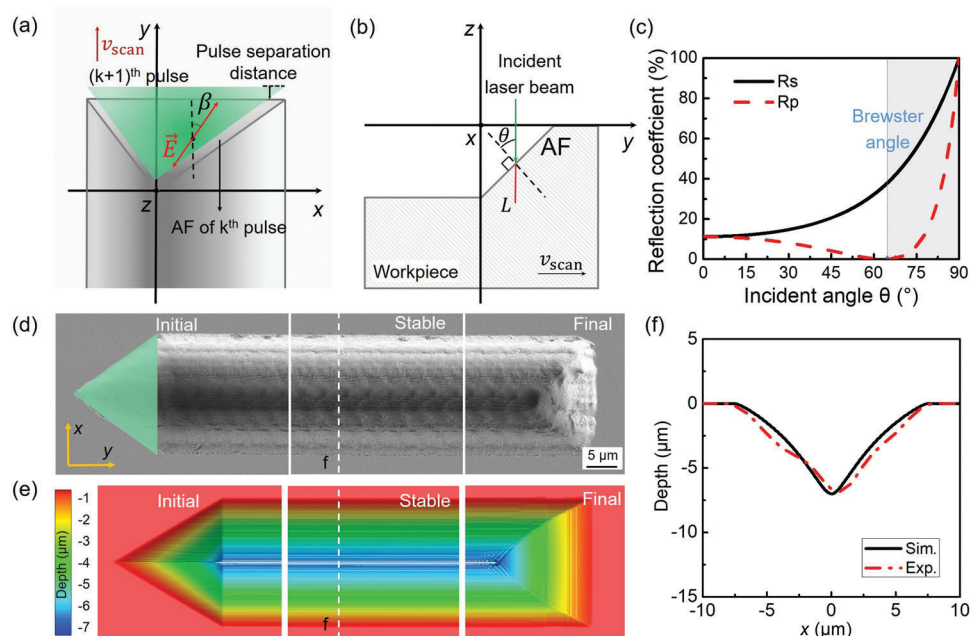
**ADVANCED
SCIENCE NEWS**

www.advancedsciencenews.com

**ADVANCED
MATERIALS
TECHNOLOGIES**

www.advmattechnol.de

Figure 2. Definition of critical parameters in LIMJAA with a triangular laser spot from a) top view and b) side view from the positive X–axis. c) Reflection coefficient of s- and p-polarization. Morphology of grooves in the initial, stable, and final stages of d) experiment and e) simulation. f) Cross-sectional profiles at the stable stage. ($f = 5$ kHz, $E = 6$ µJ, $v = 100$ µm s^{-1}, AF: ablation front).

differences is,[40]

$$R_c = R_s(\theta)\sin^2(\beta) + R_p(\theta)\cos^2(\beta) \tag{7}$$

where β is the acute angle between the normal direction of the ablation front (refers to the front end of the ablated groove seeing along the laser scanning direction) and the laser polarization direction, as shown in **Figure 2**a, θ is the incident angle of a laser beam, as marked in Figure 2b. R_s and R_p are the reflection coefficient of s- and p-polarization at the interface between a liquid film and the sample. Substituting the refractive indices of SiC and water into the Fresnel formula, R_s and R_p can be obtained, as shown in Figure 2c.

Assuming that the sample absorbs all the laser energy except the reflected part, the laser fluence for ablation can be indicated as,

$$F_A(x,y) = (1 - R_c)(1 - R_l)F(x,y) \tag{8}$$

where R_l is the reflectivity at the interface between air and liquid film.

Figure 2d,e illustrates a symmetrical triangular microgroove in the experiment and by simulation. The simulation results are almost consistent with the experimental results, which proves the effectiveness of this geometrical modeling method. The ablation process can be divided into three stages, that is, initial, stable, and final stages. A triangular cross-sectional profile similar to the beam pattern is formed in the stable stage, as shown in Figure 2f. The ablation depth at the stable stage is determined by the N_e, which is determined by the length of $h(x)$ of the laser spot as discussed in Section 2.1. The N_e in the initial or final stage is constantly changing, so the ablated cross-section is different at

each location; the cross-sections discussed in this research are all those in the stable stage.

According to the discussion and results in Section 2.1, cross-sectional profiles of microgrooves depend on the local ablation depth that is approximately proportional to $h(x)$. It must be mentioned that the polarization components of the incident laser in the ablation front affect the reflectivity on the sample and thus affect the local ablation depth as well. Therefore, exploring the influence of laser polarization and ablation front on the groove cross-sectional profiles helps design the spot shape and select laser parameters to obtain high-precision structures.

An isosceles triangular laser spot is used to process the V-shaped microgroove with two kinds of leading-edge (refers to the front end of the spot seeing along the laser scanning direction) as shown in **Figure 3**a,d, which is achieved by inverting the laser spot. The simulation results in Figure 3b,e show that the number of leading-edge results in the same number of planes on the ablation front. Figure 3c,f illustrates the effect of polarization direction on the groove shape with the two different ablation fronts. When the polarization direction is parallel or perpendicular to the laser scanning direction ($\theta_p = 0°$ or $90°$), the cross-sectional profiles of microgrooves are symmetrical triangles in both cases. If the polarization direction is neither parallel nor perpendicular to the scanning direction (such as $\theta_p = 45°$ or $-45°$ shown in Figure 3), the ablated microgrooves' shape becomes asymmetrical, as shown in Figure 3c. In contrast, the symmetry of the microgroove is not affected by the polarization direction when the ablation front is composed of only one plane in Figure 3f. The reason is that the reflectivity of s- and p-polarization is different for the incident laser when the ablation front planes are in different directions. In contrast, the reflectivity is uniform if only
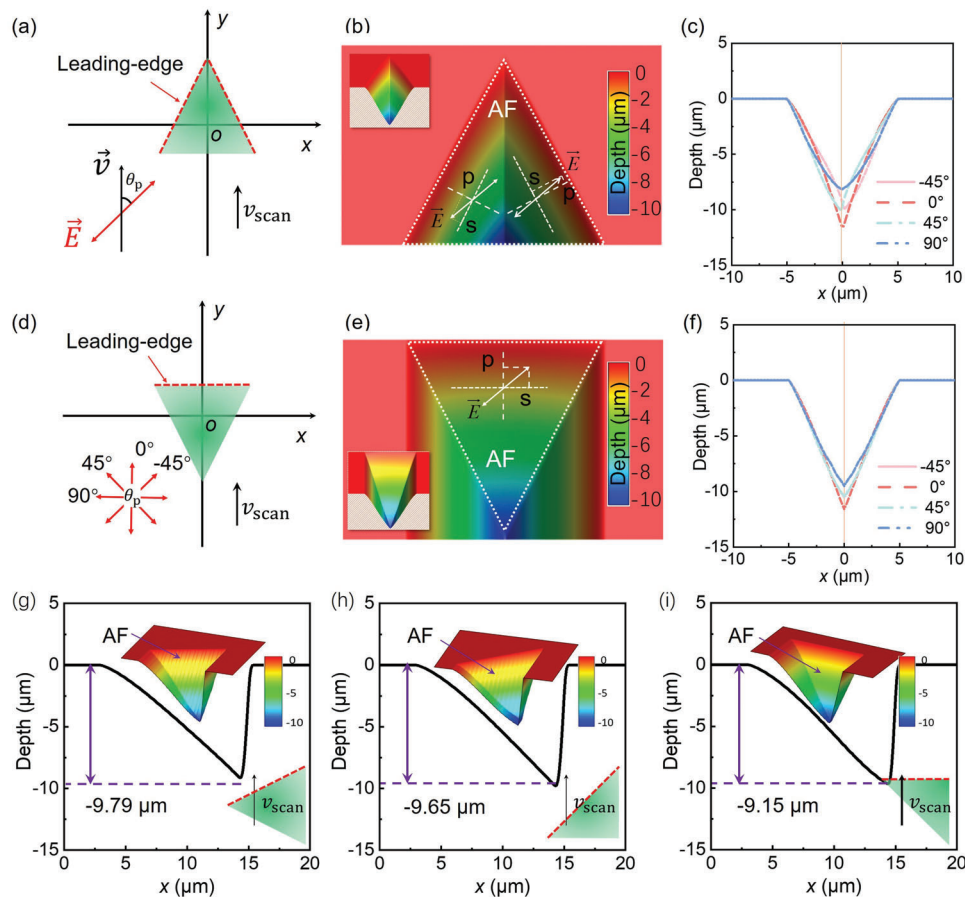
**ADVANCED
SCIENCE NEWS**

www.advancedsciencenews.com

**ADVANCED
MATERIALS
TECHNOLOGIES**

www.advmattechnol.de

Figure 3. Simulation results of laser-ablated microgrooves under different polarization and leading-edge. a,d) Schematic diagrams of laser scanning with a triangle spot with two leading-edges and one leading-edge, respectively. b,e) Top views and c,f) cross-sectional profiles of microgrooves under conditions of (a) and (d). g–i) Simulated ablation fronts and cross-sectional profiles at the stable stage of microgrooves fabricated by three distinct leading-edges. ($f = 5$ kHz, $E = 8$ µJ, $\nu = 100$ µm s^{-1}, p and s: p- and s-polarization components, AF: ablation front).

one plane exists in the ablation front. According to Equation (7), reflectivity is determined by the s- and p-polarization components of the laser beam in the ablation front, which is determined by the normal direction of the ablation front and the laser polarization. The s- and p-polarized components become different and lead to different laser energy reflectivity when the ablation front is formed by two planes, as shown in Figure 3b. Therefore, this study adopts laser spots with a single leading-edge to avoid the difference in reflectivity between multiple planes in the ablation front to get high-precision grooves. Figure 3g–i shows the microgrooves processed by three kinds of triangular laser spots with only one leading edge, while the distribution of $h(x)$ is the same. The simulation results of the ablation fronts and the cross-sectional profiles at the stable stage show that different directions of leading-edges lead to different ablation fronts but hardly affect the cross-sectional profiles of the microgrooves. These results indicate that the cross-sections of microgrooves can be designed by tuning the locally-deposited pulse energy with the specially designed distribution of $h(x)$ if laser spots with one leading edge are used. Therefore, we chose the same strategy in the following experimental study.

2.3. Effects of Spot Shape and Laser Processing Parameters on the Profile of Microgrooves

The beam shaping method can freely adjust the geometrical parameters of the laser spot, namely changing the N_e. We designed two groups of geometrical parameters by independently changing the lateral size (W) and longitudinal size (H) of the laser spot as shown in **Figure 4**, for tuning profiles of microgrooves. Since repositioning the shaping spot will cause a difference in energy distribution and change the ablation profile, the coincidence between the center of the smallest spot and the Gaussian spot is used in both experiments and simulations. Only the side length of the triangular spot is changed to study the effects of spot shape on the profile of microgrooves, as shown in Figure 4a,b insets.

The achieved cross-sectional profiles of microgrooves in experiments are shown in Figure 4c,d; the deepest position of the microgroove does not change with the change of the spot shape. The width and depth of ablated grooves under different spot shape parameters were calculated by the geometrical model, as shown in Figure 4a,b. The results show that the width is linear to W, and the depth is linear to H. Compared with the Gaussian beam, the shaped beam can independently adjust the depth and

**ADVANCED
SCIENCE NEWS**

www.advancedsciencenews.com

**ADVANCED
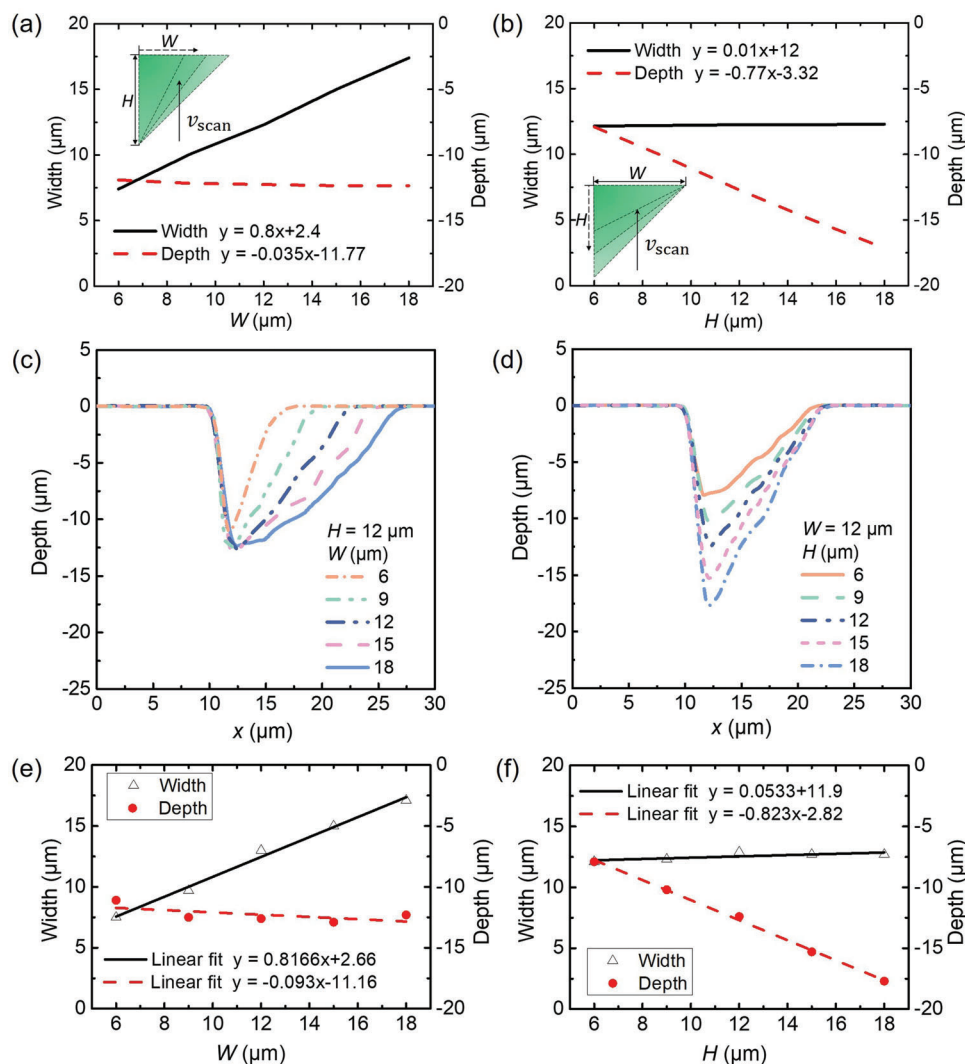MATERIALS
TECHNOLOGIES**

www.advmattechnol.de

Figure 4. Cross-sectional profiles of microgrooves fabricated by different triangular laser spots. a,b) Simulation results and c,d) experiment results with independently increasing W and H. e) and f) fitting curves of corresponding width and depth of grooves in (c) and (d). (f = 5 kHz, E = 8 µJ, v = 100 µm s^{-1}).

width of microgrooves by controlling W and H, respectively. The changing trend of corresponding widths and depths is plotted in Figure 4e,f. The experimental results are consistent with the simulation results in Figure 4a,b, verifying the effectiveness of decoupled control of the microgroove cross-sectional profiles by designing the geometric parameters of the laser spot.

The cross-sections of microgrooves are also affected by the scanning speed and single pulse energy of the patterned laser beam, as shown in **Figure 5**. Laser scanning speed hardly affects the groove width while dramatically changing the ablation depth, as shown in Figure 5a–c. It is worth noting that when the laser scanning speed is 100 µm s^{-1}, the bottom of the groove is inclined to the right, as shown in Figure 5b, which is inconsistent with the simulation result. According to Figure 2c, the sample's reflectivity increases vastly when the incident angle becomes larger than the Brewster angle. If the fluence of the reflected laser is larger than the ablation threshold, secondary ablation caused by the reflected laser beam will occur at the bottom of microgrooves, lead-

ing to the deformation of the sharp corners.[41] In this study, the secondary ablation is not considered in the geometrical model because the simulation model must traverse all the points to find the position of the secondary ablation, leading to high computation complexity. As shown in Figure 5b, this inclined sharp corner becomes faint as the speed increases to 300 µm s^{-1}. It can be attributed to the decreased reflected pulse number with smaller N_e when the scanning speed is higher.

Similarly, the varying single pulse energies will significantly change the groove depth but hardly change the groove width, as shown in Figure 5d–f. The width of the triangular microgroove can be controlled by selecting the geometric parameters of the shaped laser spot. For a Gaussian spot with an energy gradient, the ablation width will slightly increase when the single pulse energy increases because the energy at the edge of the spot gradually reaches the ablation threshold. Since our shaping spot only intercepts the energy in a small area in the center of the Gaussian spot, increasing the single pulse energy will not significantly
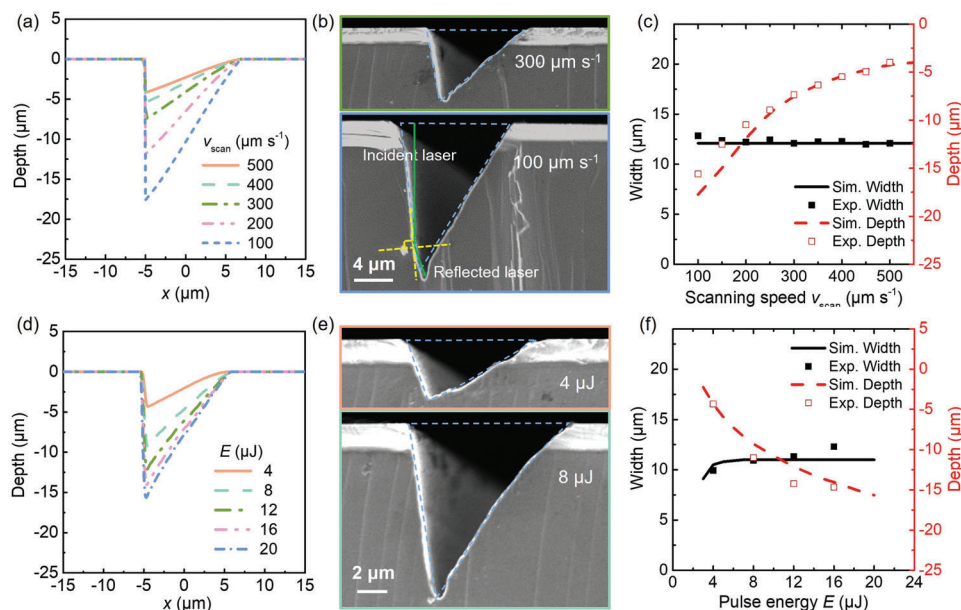
**ADVANCED
SCIENCE NEWS**

www.advancedsciencenews.com

**ADVANCED
MATERIALS
TECHNOLOGIES**

www.advmattechnol.de

Figure 5. Cross-sectional profiles of microgrooves fabricated by the same triangular laser spot. a) Simulated results with different laser scanning speeds. b) Cross-sectional images of microgrooves fabricated by laser ablation with scanning speeds of 100 and 300 µm s^{-1}, respectively. c) The influence of scanning speed on the depth and width of the microgroove; The pulse energy is 16 µJ in (a–c). d) Simulated results with increasing pulse energy. e) Cross-sectional images of microgroove fabricated by laser ablation with pulse energy of 4 µJ and 8 µJ, respectively. f) The influence of pulse energy on the depth and width of the microgroove. The laser scanning speed is 100 µm s^{-1} in (d–f). ($W = 12$ µm, $H = 12$ µm).

increase the ablation width, even though the energy density in the edge area has exceeded the ablation threshold. When N_e is constant, the locally-deposited energy depends on the pulse energy, which can also regulate the microgroove depth. However, reducing the ablation depth by lowering the pulse energy decreases the verticality of the groove wall, as the simulation and experimental results are shown in Figure 5d,e. The reason is that the phase diagram center is aligned with the center of the Gaussian beam. Laser fluence at the center of the shaped spot is highest and gradually decreases as close to the edges. When the pulse energy is small, laser fluence near the spot edge cannot cause enough ablation, reducing the verticality of the groove's left wall.

To sum up, the laser ablation method can realize the decoupled control of the width and depth of the microgroove, benefiting from the controllable locally-deposited laser energy and the intercept of the shaped spot. The width of the ablation groove is mainly determined by the lateral size W of the laser spot and does not dramatically rise when increasing the pulse energy or effective pulse number.

2.4. Variety of Machinable Microgrooves

The achievable cross-sectional profiles of microgrooves can be further broadened to W-shaped, stepped, and T-shaped ones by elaborately designed spot shapes, as shown in **Figure 6**. It has to mention that the slice in the W-shaped groove with a thickness of several micrometers is widely used as the transmission electron microscope samples after further thinning. It needs the back-and-forth switching between an electron beam and an ion beam and requires a vacuum environment to prepare a similar sample using a focused-ion beam (FIB) method.

Here, the slice can be simply fabricated within several seconds by laser ablation with linear motion of the stage. Noticeably, all the designed microgrooves can be fabricated with the same efficiency since only the local-deposited laser energy is changed. This method is also potentially applicable in manufacturing 3D multilevel microgrooves in semiconductor materials, which are traditionally fabricated by photolithography using multiple exposure processes.[42] Some unexpected strong ablation close to vertical walls at the bottom of the stepped and T-shaped grooves appears, which are caused by the secondary ablation of the reflected laser from the steep sidewalls, as the discussion of the results in Figure 5b. The undesirable secondary ablations deteriorating form accuracy of structures may be compensated by the elaborate design of the shape and polarization of the laser spot in future work.

3. Conclusions

A cross-sectional profile controllable laser micromachining method is proposed in this study for fabricating microgrooves on single crystalline silicon carbide (SiC). The effects of laser spot shape, laser polarization, and processing parameters on the cross-sections of microgrooves are systemically investigated. Compared with laser ablation in air, the patterned laser ablation in the thin liquid film is not disturbed by debris. Thus the cross-sections of microgrooves can be directly controlled by tuning the locally-deposited effective pulse number (N_e), which is designable by changing the shapes of the laser spots. In addition, the geometrical model can effectively predict cross-sectional profiles of microgrooves ablated by the patterned laser spot, which guides the design of laser spot shape and parameter selection for required cross-sections, including polarization, pulse energy,
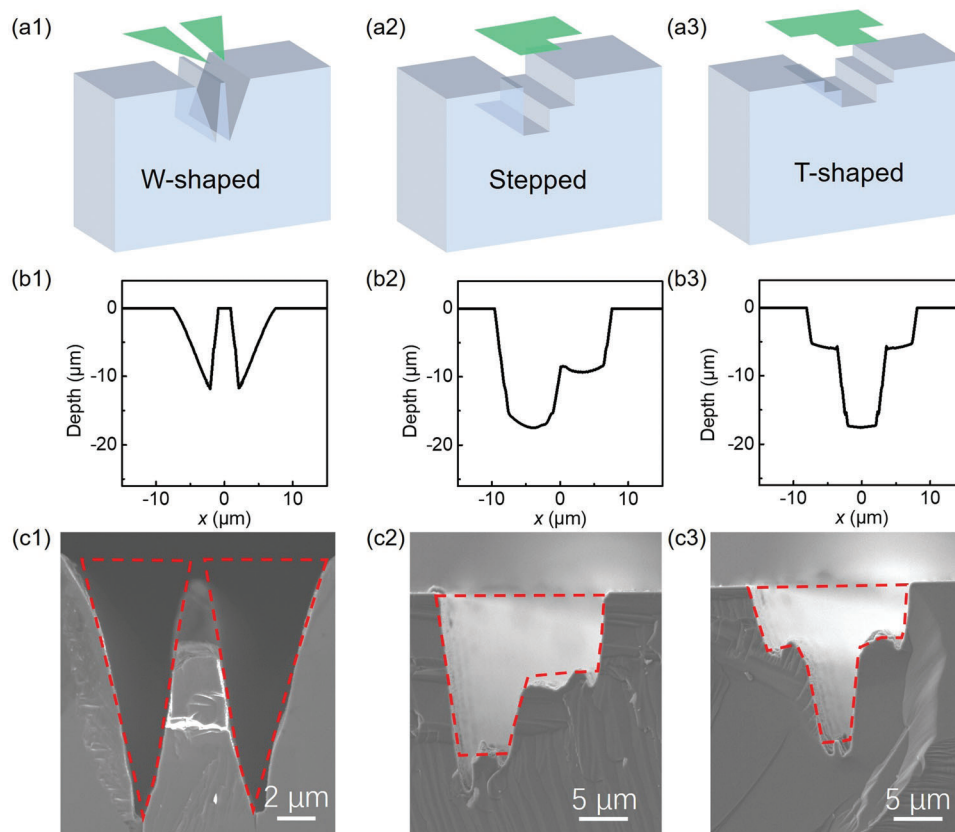
ADVANCED
SCIENCE NEWS

www.advancedsciencenews.com

ADVANCED
MATERIALS
TECHNOLOGIES

www.advmattechnol.de

Figure 6. Morphology and cross-sectional profiles of microgrooves fabricated with various laser spot shapes. a) Schematic diagrams of W-shaped, stepped, and T-shaped microgrooves. b) Simulated and c) experimental results of cross-sectional profiles.

and laser scanning strategies. Different reflectivity of polarization components on the ablation front can lead to an unwilling asymmetric shape when symmetrical microgrooves are needed, which can be solved by a patterned laser spot with only one leading-edge. This method achieves the decoupled control of the depth and width of the microgroove, in which the width is almost dependent on the maximum length of the laser spot perpendicular to the laser scanning direction, while the depth is controlled by the length distribution of the laser spot parallel to the scanning direction under fixed scanning speed and single pulse energy. The flexible achievement of microstructures, such as symmetrical V/W/T-shape microgrooves, asymmetrical V-shape microgrooves, and multilevel microgrooves, arms the laser tool with high flexibility, controllability, and efficiency to meet the complex manufacturing requirements of the modern optical-electric industry.

4. Experimental Section

Beam Shaping: A circular Gaussian beam was transformed into a geometric pattern by loading a phase diagram on a SLM (X15213 series, Hamamatsu) and cooperating with a half-wave plate and a polarizer. The laser beam shaping follows three steps. At first, a horizontally polarized laser beam goes through a half-wave plate and changes to be 45° tilted polarized. Second, an 8-bit grayscale phase diagram with a designed pattern was projected on the SLM, which induces a different phase delay (φ)

of 0 in the outer region and π in the inner region of the diagram. When a laser spot irritates the SLM, the polarization of the laser spot in the two different regions will be modulated to be orthogonal to each other. Third, a polarizer filters the outer part of the beam while the inner part remains with the desired shape. As shown in the right of Figure 1a, I_1 shows the laser polarization before modulation, and I_2–I_4 refers to the corresponding laser polarization states at three critical positions along the light path during the modulation process.

Sample Fabrication: The third-generation semiconductor material single crystalline SiC was selected as the sample as the typical difficult-to-machine material. All samples were ultrasonically cleaned with ethanol for 15 min and then washed with deionized water before and after laser processing. The patterned laser ablation experiments were performed using a femtosecond pulse laser (Spectra Physics, SpOne-8-SHG, wavelength: 520 nm and pulse width: 300 fs) with a liquid supply system. The laser repetition frequency (f) was set as 5 kHz in the experiments, which can also be increased to improve the processing efficiency. To investigate the effect of laser processing parameters on the surface structures, the single pulse energy (E) before beam shaping and the laser scanning speed (v) was varied from 4 to 16 μJ and 100 to 500 μm s^{-1}, respectively. The liquid supply system uses a low-pressure paraxial jet with a flow rate of 10 mL min^{-1} to generate a thin flowing water layer, where a waterjet nozzle was positioned above the workpiece of about 5 mm with an impinging angle of 45°. The offset distance between the laser spot and the waterjet impact position was about 3 mm, making the laser spot located in the stable thin water film area to avoid the disturbance of the hydraulic jump. A beam profiler was placed after a beam splitter to monitor the quality of the shaped beam and to make the center of the patterned spot coincide with the Gaussian spot. A CMOS camera combined with an imaging lens was used for online observation of the machining process. In the experiments,

the laser focal plane was set to be just above the sample by observing the focus of a coaxial LED with a central wavelength of 650 nm. The relative motion of the workpiece and laser spot was controlled by ultra-precision linear motor stages (Newport XMS100-S). The thickness of the liquid film in the stable area was 35.4 µm by measuring the offset of focus position as described in Figure S4, Supporting Information.

Sample Characterization: A scanning electron microscope (SEM, Zeiss Merlin) was used to measure the surface morphology of samples. A confocal 3D laser scanning microscope (CLSM, Vk-x1000, Keyence) was used to inspect the cross-sectional profiles. The samples were cut off and the cross-sectional profiles from the side view were measured for the microgrooves with large depth-to-width ratios.

Simulation Method: A geometrical model for predicting the cross-sectional profiles of microgrooves based on an ablation threshold model was established using MATLAB. The simulation of laser ablation can be established by discretizing the simulation domain into a series of evenly distributed points. The process of calculating the single-pulse laser ablation follows several steps: STEP 1: Obtain the normal vector of each point according to the surface morphology of the simulation domain; STEP 2: Calculate the incident angle (θ) and polarization angle (β) of each point according to the normal vector of the surface and the vector of laser transmission direction; STEP 3: Loop all the points; bring the θ and β of each point into Equation (7), and then calculate the comprehensive reflectance (R_c); STEP 4: R_c of each point is brought into Equation (8) to calculate the laser fluence (F_A) received by each point; STEP 5: Calculate the ablation depth (L) of each point according to Equation (3), and then move the z coordinate of each point to the negative direction according to the L. After calculating ablation depths at each point, another calculation cycle starts when the next pulse arrives and irradiates at an adjacent position with a certain pulse separation distance.

Supporting Information

Supporting Information is available from the Wiley Online Library or from the author.

Conflict of Interest

The authors declare no conflict of interest.

Data Availability Statement

The data that support the findings of this study are available in the supplementary material of this article.

[1] N. Bonod, J. Neauport, *Adv. Opt. Photonics* **2016**, *8*, 156.
[2] C. Qi, T. Chen, J. Tu, Y. Wang, *Korean J. Chem. Eng.* **2020**, *37*, 2104.
[3] W. Sun, L. Ji, Z. Lin, J. Zheng, Z. Wang, L. Zhang, T. Yan, *Adv. Funct. Mater.* **2022**, *32*, 2111920.
[4] T. Dinh, H. P. Phan, N. Kashaninejad, T. K. Nguyen, D. V. Dao, N. T. Nguyen, *Adv. Mater. Interfaces* **2018**, *5*, 1800764.
[5] T. K. Nguyen, S. Aberoumand, D. V. Dao, *Small* **2021**, *17*, 2101775.
[6] D. L. Voronov, E. M. Gullikson, H. A. Padmore, *Opt. Express* **2018**, *26*, 22011.
[7] P. Kumar, *Int. J. Therm. Sci.* **2019**, *136*, 33.
[8] J. Dou, J. Cui, X. Fang, X. Dong, N. Ullah, M. Xu, *Integr. Ferroelectr.* **2020**, *208*, 104.
[9] R. Bellazzini, M. Bozzo, A. Brez, G. Gariano, L. Latronico, N. Lumb, A. Papanestis, G. Spandre, M. M. Massai, R. Raffo, M. A. Spezziga, *Nucl. Instrum. Methods Phys. Res., Sect. A* **1999**, *424*, 444.
[10] D. Deng, Y. Xie, L. Chen, X. Chen, *Int. J Adv. Manuf. Technol.* **2019**, *101*, 9.
[11] T. Chen, A. Pan, C. Li, J. Si, X. Hou, *Appl. Surf. Sci.* **2015**, *325*, 145.
[12] Y. Huang, X. Wu, H. Liu, H. Jiang, *J. Micromech. Microeng.* **2017**, *27*, 065005.
[13] W. Wang, X. Mei, G. Jiang, S. Lei, C. Yang, *Appl. Surf. Sci.* **2008**, *255*, 2303.
[14] N. Takayama, J. Yan, *J. Mater. Process. Technol.* **2017**, *243*, 299.
[15] J. Li, Y. Tang, Z. Kuang, J. Schille, U. Loeschner, W. Perrie, D. Liu, G. Dearden, S. Edwardson, L. H. Mittweida, M. Germany, *Opt. Lasers Eng.* **2019**, *112*, 59.
[16] N. Sanner, N. Huot, E. Audouard, C. Larat, J. P. Huignard, *Opt. Lasers Eng.* **2007**, *45*, 737.
[17] H. Hocheng, K. Y. Wang, *Int. J. Manuf. Technol. Manage.* **2008**, *13*, 241.
[18] M. Pfeifer, S. Weissmantel, G. Reisse, *Appl. Phys. A: Mater. Sci. Process.* **2013**, *112*, 61.
[19] B. Jaeggi, S. Remund, R. Streubel, B. Goekce, S. Barcikowski, B. Neuenschwander, *J. Laser Micro/Nanoeng.* **2017**, *12*, 267.
[20] G. Daminelli, J. Krüger, W. Kautek, *Thin Solid Films* **2004**, *467*, 334.
[21] D. Zhang, B. Gökce, S. Sommer, R. Streubel, S. Barcikowski, *Appl. Surf. Sci.* **2016**, *367*, 222.
[22] C. Li, X. Shi, J. Si, T. Chen, F. Chen, S. Liang, Z. Wu, X. Hou, *Opt. Commun.* **2009**, *282*, 78.
[23] V. Tangwarodomnukun, J. Wang, C. Z. Huang, H. T. Zhu, *Int. J. Mach. Tools Manuf.* **2012**, *56*, 39.
[24] Y. Z. Liu, *Int. J. Mach. Tools Manuf.* **2020**, *150*, 103510.
[25] S. Duangwas, V. Tangwarodomnukun, C. Dumkum, *Mater. Manuf. Processes* **2014**, *29*, 1226.
[26] D. Kim, B. Oh, H. Lee, *Appl. Surf. Sci.* **2004**, *222*, 138.
[27] H. W. Kang, A. J. Welch, *J. Appl. Phys.* **2007**, *101*, 083101.
[28] T. T. P. Nguyen, R. Tanabe, Y. Ito, *Appl. Phys. A: Mater. Sci. Process.* **2014**, *116*, 1109.
[29] W. Lauterborn, A. Vogel, in *Bubble Dynamics and Shock Waves*, Springer, Berlin, Heidelberg **2013**, pp. 67–103.
[30] R. Timm, *J. Fluid Mech.* **1989**, *206*, 299.
[31] A. Patrascioiu, J. M. Fernández-Pradas, A. Palla-Papavlu, J. L. Morenza, P. Serra, *Microfluid. Nanofluid.* **2014**, *16*, 55.
[32] J. Long, M. H. Eliceiri, Y. Ouyang, Y. Zhang, X. Xie, C. P. Grigoropoulos, *Opt. Lasers Eng.* **2021**, *137*, 106334.
[33] Y. Guo, P. Qiu, S. Xu, G. J. Cheng, *Int. J. Extreme Manuf.* **2022**, *4*, 035101.
[34] L. Huang, K. Xu, D. Yuan, J. Hu, X. Wang, S. Xu, *Nat. Commun.* **2022**, *13*, 5823.
[35] W. Zhao, L. Wang, Z. Yu, J. Chen, J. Yang, *Opt. Laser Technol.* **2019**, *111*, 214.

[36] B. N. Chichkov, C. Momma, S. Nolte, F. von Alvensleben, A. Tünnermann, *Appl. Phys. A: Mater. Sci. Process.* **1996**, *63*, 109.

[37] N. N. Nedialkov, S. E. Imamova, P. A. Atanasov, *J. Phys. D: Appl. Phys.* **1997**, *37*, 638.

[38] S. Yan, C. Wei, H. Zou, J. Chen, Y. Li, T. Shen, A. Wang, T. Sui, B. Lin, *Ceram. Int.* **2021**, *47*, 13789.

[39] F. Di Niso, C. Gaudiuso, T. Sibillano, F. P. Mezzapesa, A. Ancona, P. M. Lugarà, *Opt. Express* **2014**, *22*, 12200.

[40] R. Wang, X. Dong, K. Wang, X. Sun, Z. Fan, W. Duan, M. Byung-Guk Jun, *Appl. Surf. Sci.* **2021**, *537*, 148001.

[41] Y. Guo, P. Qiu, S. Xu, *Opt. Express* **2022**, *30*, 44665.

[42] S. Choi, J.-K. Park, *Biomicrofluidics* **2010**, *4*, 046503.